



Cite this: *Chem. Commun.*, 2017, 53, 9542

Received 13th July 2017,
Accepted 3rd August 2017

DOI: 10.1039/c7cc05406h

rsc.li/chemcomm

Oxalate-assisted formation of uniform carbon-confined SnO₂ nanotubes with enhanced lithium storage†

Chunhua Han,^a Baoxuan Zhang,^a Kangning Zhao,^a Jiashen Meng,^a Qiu He,^a Pan He,^a Wei Yang,^a Qi Li^a and Liqiang Mai^{id}*^{ab}

SnO₂ nanotubes are synthesized via an oxalate-assisted “redox etching and precipitating” route between MnOOH nanowires and Sn²⁺ ions. The addition of oxalate is found to be crucial to guide the formation of uniform SnO₂ nanotubes. To further improve the conductivity and stability, the as-obtained SnO₂ nanotubes are coated with a thin carbon layer. The resulting carbon-confined SnO₂ nanotubes possess superior rate performance as an anode material for lithium-ion batteries.

Lithium-ion batteries (LIBs) have captured enormous attention in the field of energy storage owing to their high energy density, long lifespan and environmental benignity.^{1–4} With the increasing demand for next-generation LIBs, electrode materials with high specific capacity, long cycling stability and extraordinary rate capability are highly desired.^{5–7} Among the available anode materials for LIBs, SnO₂ has been perceived as a promising candidate due to its high theoretical capacity of 782 mA h g^{−1}, as well as appropriate working potential.^{8–10} Unfortunately, its practical application is limited by the huge volume variation during the lithium insertion/extraction process, which leads to the pulverization of active materials and formation of unstable solid–electrolyte interphase (SEI) films.^{11–14}

Two effective strategies have been proposed to address the aforementioned issues of SnO₂ anodes. One strategy is to fabricate SnO₂ with unique structures. Particularly, hollow structures with void space can not only offer abundant electrochemical active sites and a large electrode/electrolyte contact area, but also effectively prevent nanoparticles from aggregation and buffer the volume variation during cycling.^{15,16} The other strategy is to employ conformal carbon coatings, which can accommodate volume

expansion, as well as improve the electronic transport properties of electrode materials.^{8,17}

Usually, SnO₂ hollow nanostructures are synthesized by straightforward template-assisted methods.^{6,18} Typically, the desired materials or their precursors are deposited on the surface of the templates, followed by selective removal of templates via wet chemical etching or calcination.^{6,15} However, the template-assisted methods generally require high temperature and long time, or additional post-treatment for the removal of the template, which increase the cost.^{12,19} Moreover, the removal of the template may cause partial collapse of hollow nanostructures, resulting in poor uniformity of the morphology.⁶ Therefore, it is still a great challenge to fabricate well-defined SnO₂ hollow nanostructures. In recent years, the template-engaged redox etching method has been frequently adopted as an effective approach. The hollow interior is generated via the gradual oxidative/reductive dissolution of active templates, leading to the continuous formation of well-defined shell materials.¹⁶ For example, Zhao *et al.* prepared Fe(OH)₃ hierarchical nanotubes through a template-engaged redox reaction using MnOOH nanowires as the template and FeSO₄ as the iron source and reductant.²⁰

However, this method is time consuming (for 12 h) and has not been extended to the synthesis of SnO₂ nanotubes for the reason that the redox reaction between MnOOH and Sn²⁺ ions is extremely slow (Fig. S1a and b, ESI†).

Herein, we further develop a novel and efficient strategy to prepare SnO₂ nanotubes by an oxalate-assisted “redox etching and precipitating” route. The addition of oxalate is crucial for the successful formation of the SnO₂ nanotubes, through deliberately controlling the balance of the redox etching rate toward the sacrificial template and the synchronous oxidization and hydrolysis rate of Sn²⁺ ions.^{21–23} The as-prepared SnO₂ nanotubes are coated with a thin carbon layer (denoted as SnO₂@C nanotubes) and evaluated as anode materials for LIBs, which exhibit enhanced lithium storage performance.

The strategy to synthesize SnO₂ nanotubes is designed based on simultaneous redox etching of the MnOOH template and

^a State Key Laboratory of Advanced Technology for Materials Synthesis and Processing, International School of Materials Science and Engineering, Wuhan University of Technology, Wuhan 430070, Hubei, China.
E-mail: mlq518@whut.edu.cn

^b Department of Chemistry, University of California, Berkeley, California 94720, USA

† Electronic supplementary information (ESI) available. See DOI: 10.1039/c7cc05406h

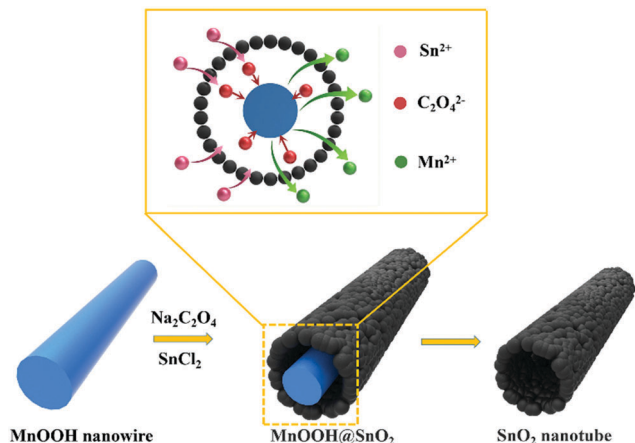
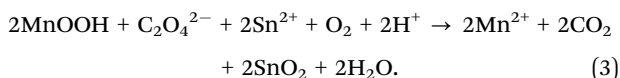
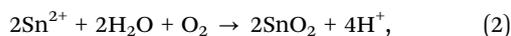
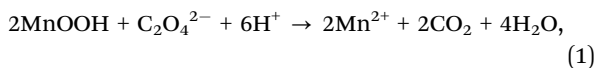


Fig. 1 Schematic illustration of the formation of SnO₂ nanotubes by an oxalate-assisted “redox etching and precipitating” route.

precisely controlled oxidation and hydrolysis of Sn²⁺ ions, as schematically illustrated in Fig. 1. The chemical route is highly anticipated to occur *via* the following reactions:^{24,25}



Oxalate is chosen as the etchant owing to the lower standard reduction potential of the CO₂/C₂O₄²⁻ pair (−0.595 V vs. SHE) than that of Sn⁴⁺/Sn²⁺ (0.154 V vs. SHE) (Table S1, ESI†). Therefore, C₂O₄²⁻ ions are easier to reduce MnOOH than Sn²⁺ ions. With the assistance of H⁺ ions, the reduction of MnOOH by C₂O₄²⁻ ions (eqn (1)) takes place on the surface of MnOOH nanowires. When the etching process occurs, the depletion of H⁺ ions can increase the pH value locally, which confines Sn²⁺ ions to the vicinity of the etching interface.^{21,23} Therefore, the oxidation and hydrolysis of Sn²⁺ ions to form the shell structure (eqn (2)) prefer to take place around the etching interface. As the reaction proceeds, MnOOH is gradually consumed while SnO₂ is preferentially deposited on the preformed SnO₂ shell in the form of nanoparticles (eqn (3)), which leads to the formation of well-defined hollow nanotubes. This process is defined as “redox etching and precipitating”. These two synchronous chemical reactions enable the exterior SnO₂ shell to perfectly inherit the morphology of the MnOOH template.²¹

The gradual removal of the MnOOH template and simultaneous formation of SnO₂ shells are monitored by time-series energy-dispersive X-ray spectroscopy (EDS) (Fig. S2, ESI†). As the reaction proceeds, the peaks of the Mn element become weaker while the peaks of the Sn element become stronger. When the reaction prolongs to 3 h, the peaks of the Mn element ultimately disappear, which indicates that the MnOOH nanowires are completely etched within 3 h. Powder X-ray diffraction (XRD) patterns (Fig. 2a and i), transmission electron microscopy (TEM) images (Fig. 2c and k) and

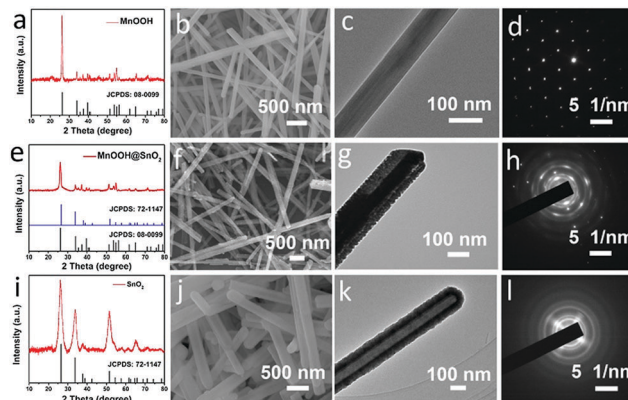


Fig. 2 (a) XRD pattern, (b) SEM image, (c) TEM image and (d) SAED pattern of the initial product; (e) XRD pattern, (f) SEM image, (g) TEM image and (h) SAED pattern of the intermediate product; (i) XRD pattern, (j) SEM image, (k) TEM image and (l) SAED pattern of the final product.

selected-area electron diffraction (SAED) patterns (Fig. 2d and l) of the initial and final products show the structural evolution from single crystal MnOOH nanowires to polycrystalline SnO₂ nanotubes. The surfaces of SnO₂ nanotubes are slightly rougher and the diameters (200–250 nm) of SnO₂ nanotubes are significantly larger (Fig. 2j) compared to those of MnOOH nanowires (Fig. 2b), which can be attributed to the formation of the SnO₂ shell *via* the accumulation of nanoparticles. It should be noted that the XRD pattern (Fig. 2e) of the intermediate product (denoted as MnOOH@SnO₂) corresponds to the MnOOH phase and the presence of SnO₂ cannot be confirmed clearly, which may be due to the similar diffraction peaks of SnO₂ and MnOOH (Fig. 2e). However, the compound phase of MnOOH@SnO₂ can be verified by the wire-in-tube structure (Fig. 2g). The SAED pattern (Fig. 2h) of MnOOH@SnO₂ including single crystal diffraction points and polycrystalline diffraction rings further confirms the above discussion.

To gain a better understanding of the formation mechanism of SnO₂ nanotubes, a set of control experiments were designed (Fig. S4, ESI†). Firstly, to demonstrate the reasonability of eqn (1) and (2), oxalate was introduced 20 min earlier than SnCl₂ (Exp. (I)). It can be seen that the brown suspension turned into a colorless and transparent solution, indicating the occurrence of eqn (1). After the addition of SnCl₂, the obtained product (denoted as Na₂C₂O₄-before) is demonstrated to be SnO₂ nanoparticles (Fig. S5a and b, ESI†), indicating the occurrence of eqn (2). In addition, to investigate the relationship of eqn (1) and (2), oxalate was not introduced in the initial 4 h of the reaction (Exp. (II)). After the addition of oxalate, it took 4 h to obtain SnO₂ with non-uniform morphology (denoted as Na₂C₂O₄-after) (Fig. S5c and d, ESI†), which shows that eqn (2) proceeded comparatively slowly before the addition of oxalate. Moreover, eqn (1) can accelerate the process of eqn (2) by consuming the H⁺ ions in the solution and induce the formation of uniform SnO₂ nanotubes. Finally, to further explore the relationship of eqn (1) and (2), an experiment was carried out under the condition of no oxygen to avoid the influence of oxygen in the air (Exp. (III)). The obtained product is demonstrated to be

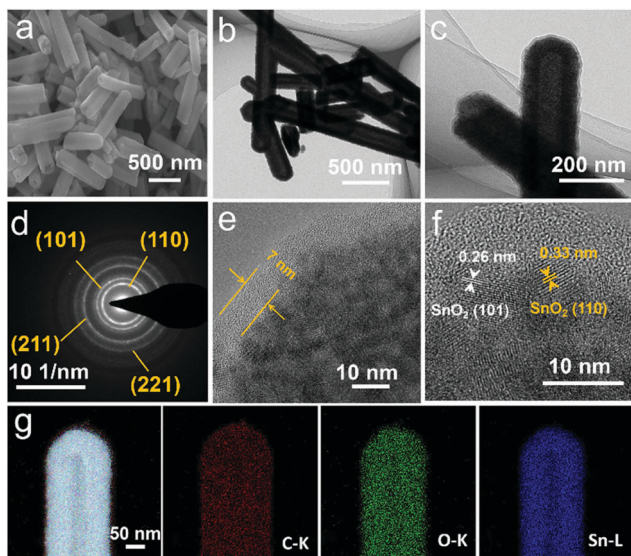


Fig. 3 (a) SEM image, (b and c) TEM images, (d) SAED pattern, (e and f) HRTEM images of SnO₂@C nanotubes; (g) STEM and corresponding elemental mapping images of an individual SnO₂@C nanotube.

unreacted MnOOH nanowires (Fig. S5e and f, ESI[†]), which indicates that eqn (1) was not thoroughly accomplished, further manifesting that H⁺ ions originating from eqn (2) can reversibly facilitate the process of eqn (1). According to the above analysis, we conclude that the formation of the SnO₂ nanotubes is based on simultaneous redox etching of the MnOOH template and precisely controlled oxidization and hydrolysis of Sn²⁺ ions. Furthermore, the timing of adding oxalate is crucial for the successful formation of SnO₂ nanotubes and eqn (1) and (2) have a relationship of mutual promotion.

To improve the electronic conductivity and structural stability, the SnO₂ nanotubes are further coated with a thin carbon layer. The scanning electron microscopy (SEM) image (Fig. 3a) shows that there is no apparent change in the morphology after carbon coating. TEM images (Fig. 3b and c) clearly indicate the hollow structure of the as-obtained SnO₂@C nanotubes. The SAED pattern (Fig. 3d) verifies the polycrystalline nature of the SnO₂@C nanotubes and the diffraction rings can be easily assigned to the SnO₂ phases. A representative high-resolution TEM image (Fig. 3e) shows that the entire surface of the SnO₂ nanotubes is coated with a continuous amorphous carbon layer with a uniform thickness of around 7 nm. The interlayer spacings are 0.33 and 0.26 nm (Fig. 3f), corresponding to the (110) and (101) planes of SnO₂, respectively.⁶ The scanning transmission electron microscopy (STEM) image and the corresponding elemental mapping images (Fig. 3g) confirm the uniform distribution of C, O, and Sn elements within the SnO₂@C nanotubes. The carbon content in the SnO₂@C nanotubes is determined to be 14.43 wt% by thermogravimetric analysis (TGA) (Fig. S6a, ESI[†]). The Raman spectrum of the SnO₂@C nanotubes (Fig. S6b, ESI[†]) contains characteristic D and G bands of carbon at approximately 1339 and 1594 cm⁻¹, respectively. The I_D/I_G ratio was found to be 0.86, demonstrating a relatively high degree of graphitization.²⁶

Furthermore, the electrochemical performances of SnO₂@C nanotubes as an anode material for LIBs were investigated. Fig. 4a shows the cyclic voltammetry (CV) curves of the first three cycles of the SnO₂@C nanotube electrodes in the voltage range of 0.01–2.5 V vs. Li/Li⁺ at a scan rate of 0.1 mV s⁻¹. The CV behaviour is in accordance with previously reported works.^{17,27–29} Specifically, the cathodic sweep of the sample in the first cycle shows a strong irreversible peak at around 0.80 V, which corresponds to the initial reduction of SnO₂ and the formation of SEI films. The clearly discerned reductive peak near 0.14 V can be attributed to the formation of the Li_xSn alloy. Meanwhile, in the anodic process of the first cycle, a strong peak at 0.54 V and a broad peak at 1.23 V can be associated with the dealloying process of Li_xSn and partial reversible conversion of Sn/Li₂O to SnO₂, respectively. The representative charge–discharge profiles of the sample are shown in Fig. 4b. Two pairs of poorly defined plateaus can be identified during the initial charge and discharge, which are in good agreement with the CV result. The initial discharge and charge capacities are 1723 and 1140 mA h g⁻¹, respectively, corresponding to an initial Coulombic efficiency of 66%. Fig. 4c shows the cycling performance of SnO₂@C nanotubes at a current density of 500 mA g⁻¹ in the voltage window from 0.01 to 2.0 V vs. Li/Li⁺. The discharge capacity of the 100th cycle

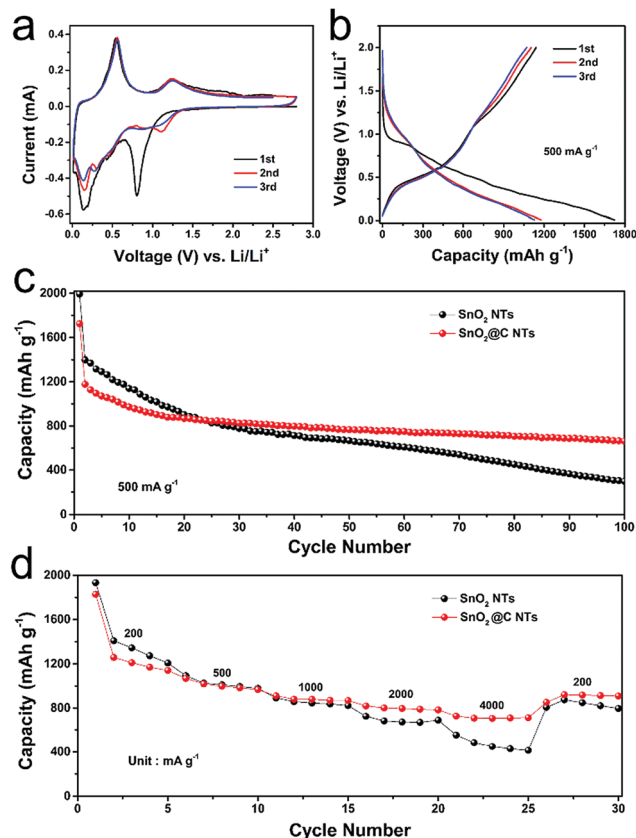


Fig. 4 (a) CV curves of the first three cycles between 0.01 and 2.5 V at a scan rate of 0.1 mV s⁻¹, (b) charge–discharge voltage profiles at a current density of 500 mA g⁻¹ of the SnO₂@C nanotube electrodes; (c) cycling performance at a current density of 500 mA g⁻¹, and (d) rate capability of SnO₂ nanotubes and SnO₂@C nanotubes.

is 663 mA h g⁻¹. Furthermore, the SnO₂@C nanotubes sample is tested at various current densities ranging from 200 to 4000 mA g⁻¹ to evaluate the rate capability (Fig. 4d). The SnO₂@C nanotubes deliver average discharge capacities of 1195, 1007, 882, 798, and 711 mA h g⁻¹ at current densities of 200, 500, 1000, 2000, and 4000 mA g⁻¹, respectively. When the current density is finally decreased to 200 mA g⁻¹, an average discharge capacity as high as 903 mA h g⁻¹ can be restored. To make a clear comparison, the electrochemical performance of the SnO₂ nanotubes has also been examined (Fig. 4c and d). Under the same test conditions, SnO₂ nanotubes deliver much more rapid capacity fading. It is worth noting that the initial discharge capacities of SnO₂ nanotubes are higher than those of SnO₂@C nanotubes, which is because the addition of a carbon coating layer would pay the price of decreasing the total capacity.²⁰

SnO₂@C nanotubes exhibit superior rate capability when compared with some other SnO₂-based nanostructures (Table S2, ESI[†]), which can be attributed to the following aspects. On one hand, the hollow nanostructure of SnO₂ nanotubes gives rise to a relatively high surface area of 120.23 m² g⁻¹ (Fig. S7a, ESI[†]), which can render a large electrode/electrolyte contact area for Li⁺ ion diffusion.¹¹ On the other hand, the conformal thin carbon coating can increase the electronic conductivity of the SnO₂ nanotubes and facilitate the electronic transport. An electrochemical impedance spectroscopy (EIS) plot (Fig. S7b, ESI[†]) shows that SnO₂@C nanotubes have a smaller diameter of the high-frequency semicircle than the bare SnO₂ nanotubes, suggesting a lower charge transfer resistance.¹¹ Moreover, both the hollow tubular structure and carbon coating can buffer the huge volume variation during repeated charge–discharge cycling and thus guarantee the structural integrity of SnO₂@C nanotubes. The SEM image (Fig. S7c, ESI[†]) of SnO₂@C nanotubes after cycling 100 times at 500 mA g⁻¹ shows that the original shape can be generally preserved. Benefiting from the hollow tubular structure and thin carbon coating, the SnO₂@C nanotubes exhibit excellent rate capability.

In summary, we present a novel design for the synthesis of SnO₂ nanotubes by an oxalate-assisted “redox etching and precipitating” route. The formation mechanism which is based on simultaneous redox etching of the MnOOH template and precisely controlled oxidization and hydrolysis of Sn²⁺ has been revealed. The addition of oxalate is found to be crucial to guide the formation of uniform SnO₂ nanotubes. Furthermore, the resulting carbon-confined SnO₂ nanotube electrodes show superior rate performance as an anode material for LIBs. We believe that the unique synthesis route presented in this work can be extended to other metal oxides, and will shed some light on designing of well-defined hollow nanostructures.

This work was supported by the National Key Research and Development Program of China (2016YFA0202603), the National Basic Research Program of China (2013CB934103), the Programme

of Introducing Talents of Discipline to Universities (B17034), the National Natural Science Foundation of China (51521001), the National Natural Science Fund for Distinguished Young Scholars (51425204), and the Fundamental Research Funds for the Central Universities (WUT: 2016III001, 2017III009). Prof. Liqiang Mai gratefully acknowledges financial support from the China Scholarship Council (No. 201606955096).

Notes and references

- 1 D. Wang, J. Yang, X. Li, D. Geng, R. Li, M. Cai, T.-K. Sham and X. Sun, *Energy Environ. Sci.*, 2013, **6**, 2900.
- 2 J. Liang, X. Y. Yu, H. Zhou, H. B. Wu, S. Ding and X. W. Lou, *Angew. Chem., Int. Ed.*, 2014, **53**, 12803–12807.
- 3 L. Ji, Z. Lin, M. Alcoutlabi and X. Zhang, *Energy Environ. Sci.*, 2011, **4**, 2682.
- 4 M. V. Reddy, G. V. Subba Rao and B. V. Chowdari, *Chem. Rev.*, 2013, **113**, 5364–5457.
- 5 Y. Yu, L. Gu, C. Wang, A. Dhanabalan, P. A. van Aken and J. Maier, *Angew. Chem., Int. Ed.*, 2009, **48**, 6485–6489.
- 6 Y. L. Ding, Y. Wen, P. A. van Aken, J. Maier and Y. Yu, *Nanoscale*, 2014, **6**, 11411–11418.
- 7 Z. Zhu, S. Wang, J. Du, Q. Jin, T. Zhang, F. Cheng and J. Chen, *Nano Lett.*, 2014, **14**, 153–157.
- 8 J. S. Chen and X. W. Lou, *Small*, 2013, **9**, 1877–1893.
- 9 K. Zhao, L. Zhang, R. Xia, Y. Dong, W. Xu, C. Niu, L. He, M. Yan, L. Qu and L. Mai, *Small*, 2016, **12**, 588–594.
- 10 C. Guan, X. Wang, Q. Zhang, Z. Fan, H. Zhang and H. J. Fan, *Nano Lett.*, 2014, **14**, 4852–4858.
- 11 X. Zhou, L. Yu and X. W. Lou, *Adv. Energy Mater.*, 2016, **6**, 1600451.
- 12 L. Yang, T. Dai, Y. Wang, D. Xie, R. L. Narayan, J. Li and X. Ning, *Nano Energy*, 2016, **30**, 885–891.
- 13 X. Zhou, L. J. Wan and Y. G. Guo, *Adv. Mater.*, 2013, **25**, 2152–2157.
- 14 V. Raju, X. Wang, W. Luo and X. Ji, *Chem. – Eur. J.*, 2014, **20**, 7686–7691.
- 15 L. Yu, H. Hu, H. B. Wu and X. W. Lou, *Adv. Mater.*, 2017, **29**, 1604563.
- 16 G. Gao, L. Yu, H. B. Wu and X. W. Lou, *Small*, 2014, **10**, 2515.
- 17 S. Chen, Y. Xin, Y. Zhou, F. Zhang, Y. Ma, H. Zhou and L. Qi, *J. Mater. Chem. A*, 2014, **2**, 15582–15589.
- 18 M. Lai, J. H. Lim, S. Mubeen, Y. Rheem, A. Mulchandani, M. A. Deshusses and N. V. Myung, *Nanotechnology*, 2009, **20**, 185602.
- 19 W.-S. Kim, B.-S. Lee, D.-H. Kim, H.-C. Kim, W.-R. Yu and S.-H. Hong, *Nanotechnology*, 2010, **21**, 245605.
- 20 K. Zhao, M. Wen, Y. Dong, L. Zhang, M. Yan, W. Xu, C. Niu, L. Zhou, Q. Wei, W. Ren, X. Wang and L. Mai, *Adv. Energy Mater.*, 2017, **7**, 1601582.
- 21 J. Nai, Y. Tian, X. Guan and L. Guo, *J. Am. Chem. Soc.*, 2013, **135**, 16082–16091.
- 22 Z. Wang, D. Luan, F. Y. Boey and X. W. Lou, *J. Am. Chem. Soc.*, 2011, **133**, 4738–4741.
- 23 Z. Wang, D. Luan, C. M. Li, F. Su, S. Madhavi, F. Y. Boey and X. W. Lou, *J. Am. Chem. Soc.*, 2010, **132**, 16271–16277.
- 24 Z. Wang, Z. Wang, S. Madhavi and X. W. Lou, *J. Mater. Chem.*, 2012, **22**, 2526–2531.
- 25 A. G. Xyla, B. Sulzberger, G. W. L. Iii, J. G. Hering, P. V. Cappellen and W. Stumm, *Langmuir*, 1992, **8**, 95–103.
- 26 J. S. Cho, Y. J. Hong and Y. C. Kang, *ACS Nano*, 2015, **9**, 4026.
- 27 X. Hu, G. Zeng, J. Chen, C. Lu and Z. Wen, *J. Mater. Chem. A*, 2017, **5**, 4535–4542.
- 28 D. Pan, N. Wan, Y. Ren, W. Zhang, X. Lu, Y. Wang, Y. S. Hu and Y. Bai, *ACS Appl. Mater. Interfaces*, 2017, **9**, 9747–9755.
- 29 W. Dong, J. Xu, C. Wang, Y. Lu, X. Liu, X. Wang, X. Yuan, Z. Wang, T. Lin, M. Sui, I. W. Chen and F. Huang, *Adv. Mater.*, 2017, **29**, 1700136.